

REGULAR PAPERS

## Accuracy improvement in measurement of arterial wall elasticity by applying pulse inversion to phased-tracking method

To cite this article: Yukiya Miyachi *et al* 2018 *Jpn. J. Appl. Phys.* **57** 07LF08

View the [article online](#) for updates and enhancements.



## Accuracy improvement in measurement of arterial wall elasticity by applying pulse inversion to phased-tracking method

Yukiya Miyachi<sup>1,2\*</sup>, Mototaka Arakawa<sup>2,3</sup>, and Hiroshi Kanai<sup>3,2</sup>

<sup>1</sup>Medical Systems Research and Development Center R&D Management Headquarters, FUJIFILM Corporation, Kaisei, Kanagawa 258-8538, Japan

<sup>2</sup>Graduate School of Biomedical Engineering, Tohoku University, Sendai 980-8579, Japan

<sup>3</sup>Graduate School of Engineering, Tohoku University, Sendai 980-8579, Japan

\*E-mail: yukiya.miyachi@fujifilm.com

Received November 5, 2017; revised February 2, 2018; accepted February 27, 2018; published online June 5, 2018

In our studies on ultrasonic elasticity assessment, minute change in the thickness of the arterial wall was measured by the phased-tracking method. However, most images in carotid artery examinations contain multiple-reflection noise, making it difficult to evaluate arterial wall elasticity precisely. In the present study, a modified phased-tracking method using the pulse inversion method was examined to reduce the influence of the multiple-reflection noise. Moreover, aliasing in the harmonic components was corrected by the fundamental components. The conventional and proposed methods were applied to a pulsated tube phantom mimicking the arterial wall. For the conventional method, the elasticity was 298 kPa without multiple-reflection noise and 353 kPa with multiple-reflection noise on the posterior wall. That of the proposed method was 302 kPa without multiple-reflection noise and 297 kPa with multiple-reflection noise on the posterior wall. Therefore, the proposed method was very robust against multiple-reflection noise. © 2018 The Japan Society of Applied Physics

### 1. Introduction

Along with the recent changes in lifestyle in Japan, the incidence of coronary artery disease has increased steadily.<sup>1)</sup> Atherosclerosis is considered to be the main cause of coronary artery disease. Since there are significant differences in elasticity between normal and atherosclerotic arterial walls,<sup>2,3)</sup> it is effective to evaluate the elasticity of the arterial wall.<sup>4)</sup> Many studies have shown that some markers can be noninvasively measured for the detection of atherosclerosis such as the intima-media thickness (IMT) of the arterial wall, pulse wave velocity (PWV), and the elasticity of the arterial wall.

IMT is measured accurately as the average distance between the lumen-intima boundary and the media-adventitia boundary from a B-mode ultrasonic image.<sup>5-11)</sup> Carotid IMT is widely used as a surrogate marker of atherosclerosis worldwide. However, a conventional B-mode ultrasonic image provides only information on shape, and mechanical properties such as arterial wall elasticity cannot be evaluated.

PWV is a measure of the arterial pulse propagating through the circulatory system. PWV is used clinically as a noninvasive diagnostic tool for the measurement of the elasticity of the arterial wall.<sup>12-14)</sup> Although it is useful for the evaluation of global elasticity such as from the heart to the peripheral artery, regional elasticity has not been evaluated.

In a series of studies,<sup>15-31)</sup> the elasticity of a local region has been obtained by the ultrasonic phased-tracking method. In these studies, the displacement and change in the thickness of the arterial wall caused by the heartbeat have been measured. The elasticity of the human carotid artery is obtained from the measured change in thickness and the blood pressure. In these methods, to track the fast movement of the human carotid arterial wall, a high frame rate, of at least 100 Hz, is necessary. These methods can be used to evaluate the elasticity precisely when images are clear.

However, unfortunately, most images in a clinical setting contain various types of noise, such as multiple-reflection noise, making it difficult to measure the movement of the carotid arterial wall and evaluate its elasticity precisely.

To suppress the multiple-reflection noise, tissue harmonic imaging is widely used in carotid artery examinations.<sup>32,33)</sup> The pulse inversion (PI) method is one of the tissue harmonic imaging techniques and is preferred for obtaining more broadband images.<sup>34-38)</sup> Although the multiple-reflection noise is significantly improved, the frame rate of the PI method is reduced to half.

In the present study, we propose a modified phased-tracking method using the PI method for reducing the influence of multiple-reflection noise on the estimation of elasticity. To avoid aliasing of the phase shift of harmonic signals owing to the reduced frame rate, fundamental signals are also used to correct the aliasing of the phase shift. Improvement of accuracy by the proposed method was validated using the silicone rubber tube phantom.

### 2. Methods

#### 2.1 Phased-tracking method

To obtain a small change in thickness of the arterial wall, which is defined as the difference between the displacement  $\Delta h(t)$  of the intima-lumen boundary  $x_{in}(t)$  and that of the adventitia-media boundary  $x_{ad}(t)$ , the velocities  $v_{in}(t)$  and  $v_{ad}(t)$  on the intima-lumen boundary and adventitia-media boundary, respectively, are measured by the following phased-tracking method.<sup>15,16)</sup>

Ultrasonic pulses are transmitted at the pulse repetition interval  $T_r$  from the transducer on the surface of the skin. The pulse reflected from the object is received, amplified, and converted to a digital signal. Quadrature demodulation is applied to the digital signal. Using the quadrature demodulated signal  $z(t; d)$  reflected from depth  $d$  at a time  $t$ , the phase shift  $\Delta\Psi_f(t)$  between echoes in two consecutive frames is estimated from the following complex cross-correlation function:

$$\exp(j\Delta\hat{\psi}_i(t)) = \frac{\sum_{m=-M_C/2}^{M_C/2} z(t + T_r; x_i(t) + mD) \cdot z^*(t; x_i(t) + mD)}{\left| \sum_{m=-M_C/2}^{M_C/2} z(t + T_r; x_i(t) + mD) \cdot z^*(t; x_i(t) + mD) \right|}, \quad (1)$$

where  $D$  is the interval of sampled points in the depth direction,  $i$  denotes the intima–lumen boundary or adventitia–media boundary,  $x_i(t)$  denotes the displacement of these boundaries, and  $*$  represents the complex conjugate, respectively. In Eq. (1), the number of sampled points,  $M_C + 1$ , is determined by considering the received pulse length. The  $\hat{\psi}_i(t)$  above  $\Delta\hat{\psi}_i(t)$  denotes the estimate of the variable (the phase shift). In the estimation of the phase shift by Eq. (1), the object position is tracked by integration of the average velocity,  $v_i(t + T_r/2)$ , during the pulse repetition interval  $T_r$  as follows:

$$\begin{aligned} \hat{x}_i(t + T_r) &= \hat{x}_i(t) + \hat{v}_i\left(t + \frac{T_r}{2}\right) \times T_r \\ &= \hat{x}_i(t) + \frac{c_0}{2\omega_0} \Delta\hat{\psi}_i(t) \times T_r, \end{aligned} \quad (2)$$

where  $\omega_0$  and  $c_0$  are the center angular frequency of the quadrature phase detection and the speed of sound, respectively. From the displacement  $x_i(t)$ , the small change in thickness,  $\Delta h(t)$ , of the arterial wall is given by

$$\begin{aligned} \Delta h(t) &= x_{in}(t) - x_{ad}(t) \\ &= \int_0^t [v_{in}(t) - v_{ad}(t)] dt. \end{aligned} \quad (3)$$

From the ratio of the maximum decrease in thickness during a cardiac cycle,  $\Delta h_{max} = \max_t |\Delta h(t)|$ , to the maximum thickness,  $h(0)$ , the maximum strain is obtained by  $\Delta\epsilon_{max} = \Delta h_{max}/h(0)$ . By assuming that the arterial wall is incompressible and that the blood pressure applied to the arterial wall is normal, the elastic modulus  $E_\theta$  is approximately given by<sup>21)</sup>

$$E_\theta = \frac{3}{8} \left(1 + \frac{2r_0}{h(0)}\right) \frac{\Delta p}{\Delta\epsilon_{max}}, \quad (4)$$

where  $r_0$  and  $\Delta p$  are respectively the inner radius at the maximum thickness timing and the pulse pressure, which is the difference of the systolic blood pressure from the diastolic blood pressure measured at the upper arm.

Experiments were conducted using ultrasonic diagnostic equipment (Fujifilm FC1) with a linear-type transducer, and the quadrature demodulated signals were saved as raw data. The transmitting and detection center frequencies were set to 11.4 and 11 MHz, respectively. The frame rate and sampling interval of the quadrature demodulated signal were 200 Hz and 0.056 mm, respectively.

Figure 1(a) shows a magnified M-mode image of the common carotid artery obtained from a healthy 44-year-old male with the posterior wall boundary tracking results overlaid. Figures 1(b), 1(c), and 1(d) show the phase shift at the intima–lumen boundary, the phase shift at the adventitia–media boundary, and the change in the thickness of the posterior wall, respectively. In Fig. 1(d), at the time when the posterior wall was closest to the transducer, the change in thickness is set to zero. Using these results,  $E_\theta$  was estimated as 271 kPa using Eq. (4).

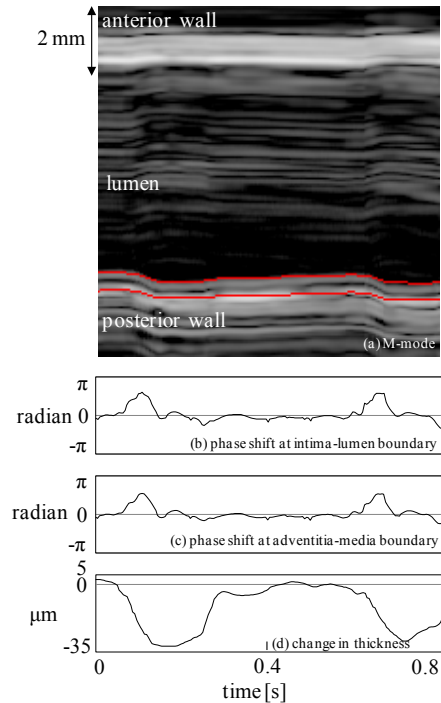


**Fig. 1.** (Color online) Carotid artery results without the multiple-reflection noise on the posterior wall. (a) Magnified M-mode with the posterior wall boundary tracking results overlaid. (b) Phase shift at the intima–lumen boundary. (c) Phase shift at the adventitia–media boundary. (d) Change in thickness of the posterior wall.

However, almost all ultrasonography images taken in a clinical setting of the carotid artery contain various types of noise, such as multiple-reflection noise, making it difficult to evaluate arterial wall elasticity precisely. For example, Fig. 2(a) shows a magnified M-mode image where the multiple-reflection noise from the anterior wall was overlaid on the posterior wall. The subject is the same as that for the image shown Fig. 1, but the transducer position was changed to generate multiple-reflection noise from the anterior wall. Figures 2(b)–2(d) show the phase shift at the intima–lumen boundary, the phase shift at the adventitia–media boundary, and the change in thickness of the posterior wall, respectively. Figure 2(d) shows that the shape of change in thickness did not correspond to heartbeat, and the maximum change in thickness was relatively smaller than that in Fig. 1(d). Using these results,  $E_\theta$  was estimated as 753 kPa using Eq. (4). Comparison of the results in Fig. 1 with those in Fig. 2 shows that the multiple-reflection noise could decrease the accuracy of the measured elasticity.

## 2.2 Pulse inversion method

In B-mode imaging, tissue harmonic imaging has been shown to reduce noise and improve image quality. Tissue harmonic imaging utilizes the harmonic signals generated during acoustic propagation through soft tissues. The following two methods are commonly used to obtain the

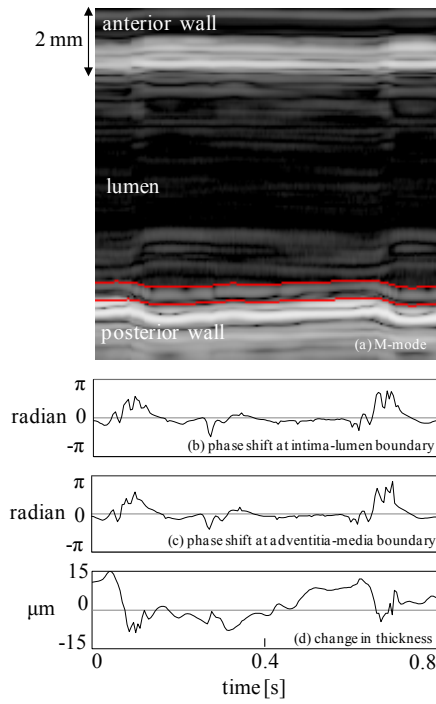


**Fig. 2.** (Color online) Carotid artery results with the multiple-reflection noise on the posterior wall. (a) Magnified M-mode image with the posterior wall boundary tracking results overlaid. (b) Phase shift at the intima–lumen boundary. (c) Phase shift at the adventitia–media boundary. (d) Change in thickness of the posterior wall.

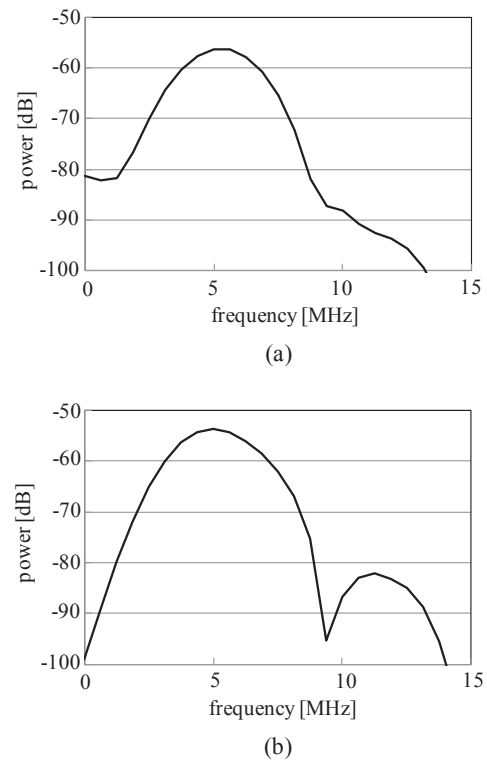


**Fig. 4.** Power spectra. (a) RF echo reflected from the multiple-reflection noise in the lumen. (b) RF echo reflected from the intima-media complex.

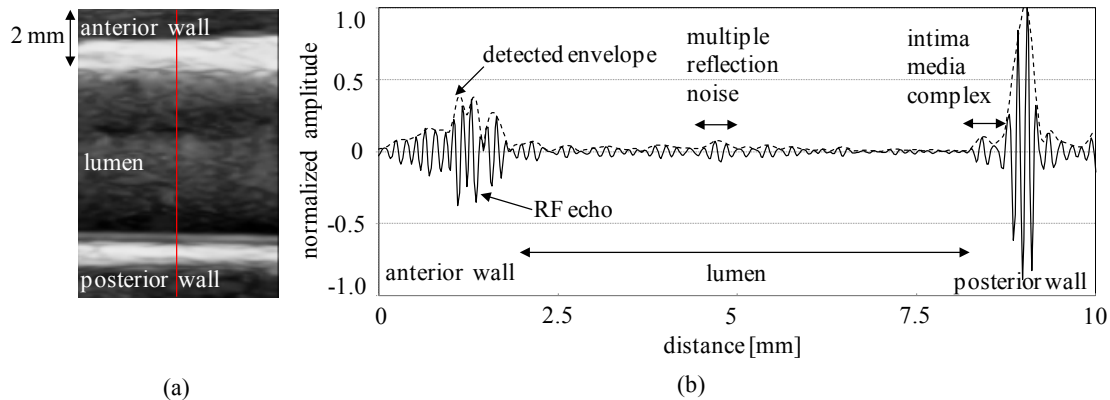


**Fig. 3.** (Color online) Magnified B-mode image and RF echo from the carotid artery. (a) Magnified B-mode image. (b) RF echo along the red vertical line shown in (a).

harmonic signals. The first is the filtered method, where a bandpass filter is used to select the harmonic components from the received signals. The second is the PI method, where two pulses with opposite polarities are transmitted and then are summed to cancel the fundamental components while the harmonics double. Since the transducer bandwidth is limited, the PI method is widely used to obtain broadband harmonic signals.

Figure 3(a) shows the B-mode image obtained by the PI method for the common carotid artery and Fig. 3(b) shows the received RF echo along the red vertical line in Fig. 3(a). The dotted line is the detected envelope of the RF echo in Fig. 3(b). The transmitting center frequency and the sampling frequency of the received echo were set to 5.7 and 40 MHz, respectively. Figures 4(a) and 4(b) show the power spectrum of the RF echo reflected from the multiple-reflection noise in

the lumen and that of the RF echo reflected from the intima-media complex (IMC), which was extracted using a Hanning window at the position shown in Fig. 3(b). In Fig. 4(a), only one peak appeared at approximately 5 MHz, which corresponds to the fundamental components of the transmitting frequency of 5.7 MHz. In Fig. 4(b), not only the peak at around 5 MHz but also a subpeak at around 11 MHz, which corresponds to the harmonic components of the transmitting frequency of 5.7 MHz, were observed. The multiple reflection noise tends to be more attenuated than single-reflection signals because it is reflected more than once. This could be the reason that the harmonic component cannot be observed in the multiple-reflection noise in Fig. 4(a). This reason is discussed in detail in Sect. 4. From these results, 11 MHz was chosen as the center detection frequency for the selection of harmonic components and 5.5 MHz was chosen as a center

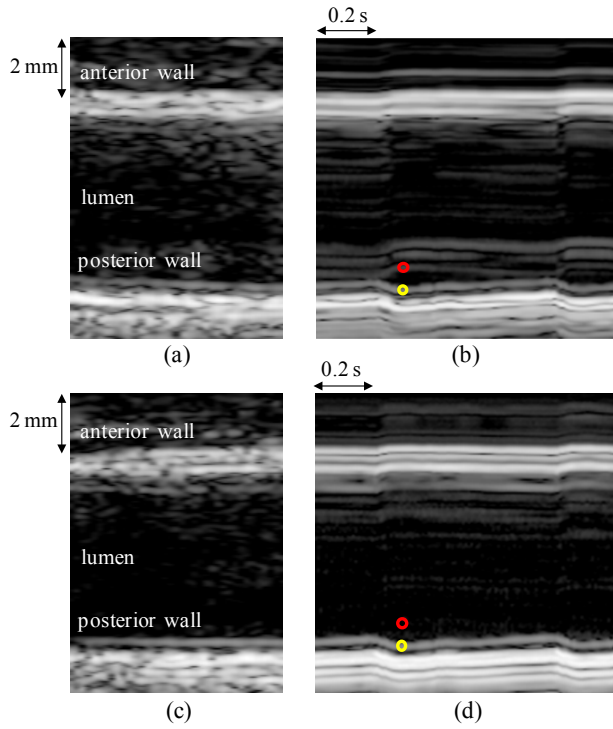


**Fig. 5.** (Color online) B-mode and M-mode images of the fundamental and the PI method at carotid artery. (a) B-mode image of the fundamental method. (b) M-mode image of the fundamental method. (c) B-mode image of the PI method. (d) M-mode image of the PI method.

detection frequency for the selection of fundamental components in Sect. 3.

B-mode and M-mode carotid artery images obtained by the fundamental method, in which the transmitting center frequency was set at 11.4 MHz and the center detection frequency was set at 11 MHz, are shown in Figs. 5(a) and 5(b), respectively. On the other hand, B-mode and M-mode images obtained by the PI method, in which transmitting center frequency was set at 5.7 MHz and the center detection frequency was set at 11 MHz, are shown in Figs. 5(c) and 5(d), respectively. The signal-to-noise ratios defined by the signal from IMC yellow circles in Figs. 5(b) and 5(d) and the multiple-reflection noise red circles in Figs. 5(b) and 5(d) were 9 dB for the fundamental method and 20 dB for the PI method. Apparently, the PI method was superior to the fundamental method from the viewpoint of reduction of the multiple-reflection noise.

### 2.3 Applying pulse inversion to phased-tracking method

Although the PI method improves the signal-noise ratio, the frame rate was reduced by half because two pulses are needed to create a single harmonic echo. Reduced frame rate tends to result in aliasing of the phase shift and tracking error because of rapid arterial wall motion. In the present study, to avoid the aliasing of the phase shift of harmonic components, the fundamental components, subtracted from the two pulses, were employed to correct the phase shift of the harmonic components. Figure 6 shows an outline of the PI method used this study. As discussed in the previous section, the transmitting center frequency of the pairs of inverted pulses was 5.7 MHz. To obtain harmonic quadrature demodulated signals, by summing pairs of received echo, the fundamental components were canceled while the harmonic components were doubled. Summed RF data were dominant at a center frequency of 11 MHz. On the other hand, to obtain the fundamental quadrature demodulated signals, by subtracting pairs of the received echo, the harmonic components were canceled while the fundamental components became double. Subtracted RF data were dominant at the center frequency of 5.5 MHz.

The phase shift of the harmonic quadrature demodulated signal  $\theta_{\text{harm}}$  was roughly equal to  $(f_{\text{harm}}/f_{\text{fund}}) \times \theta_{\text{fund}}$ , where  $f_{\text{harm}}$ ,  $f_{\text{fund}}$ , and  $\theta_{\text{fund}}$  are the harmonic detection center frequency, the fundamental detection center frequency, and the phase shift of the fundamental quadrature demodulated signal, respectively.  $\theta_{\text{harm}}$  is roughly equal to  $2\theta_{\text{fund}}$  because  $f_{\text{harm}}$  is 11 MHz and  $f_{\text{fund}}$  is 5.5 MHz in the present study. Since the purpose of this correction is to compensate for the reduction of the frame rate by half originating from the PI method, only first aliasing of  $\theta_{\text{harm}}$  is corrected using  $\theta_{\text{fund}}$ . To correct aliasing of the phase shift of the harmonic signals, firstly the aliasing number candidate  $n$  is evaluated by

$$\begin{aligned}
 -\pi &\leq \theta_{\text{fund}} < -\frac{\pi}{2} - W \Rightarrow n = -1, \\
 -\frac{\pi}{2} - W &\leq \theta_{\text{fund}} < -\frac{\pi}{2} + W \Rightarrow n = 0 \text{ or } -1, \\
 -\frac{\pi}{2} + W &\leq \theta_{\text{fund}} < \frac{\pi}{2} - W \Rightarrow n = 0, \\
 \frac{\pi}{2} - W &\leq \theta_{\text{fund}} < \frac{\pi}{2} + W \Rightarrow n = 0 \text{ or } 1, \\
 \frac{\pi}{2} + W &\leq \theta_{\text{fund}} < \pi \Rightarrow n = 1,
 \end{aligned} \tag{5}$$

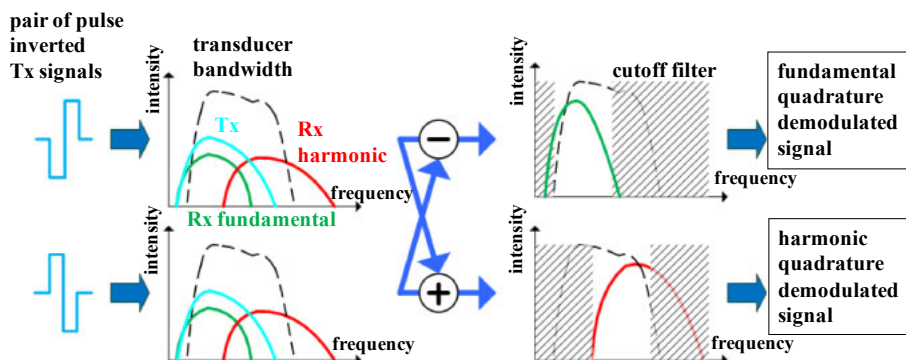


**Fig. 6.** (Color online) Outline of the PI method in this study.

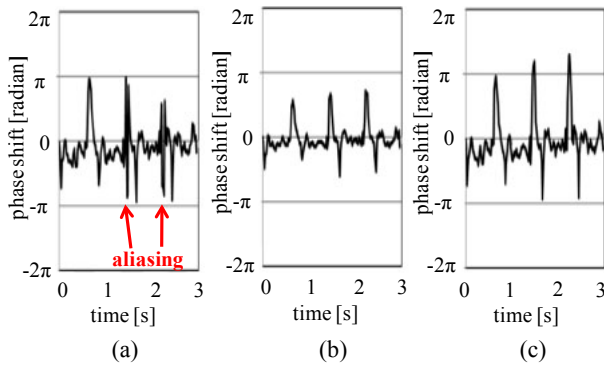


**Fig. 7.** (Color online) Phase shifts of the (a) harmonic, (b) fundamental and (c) corrected harmonic.

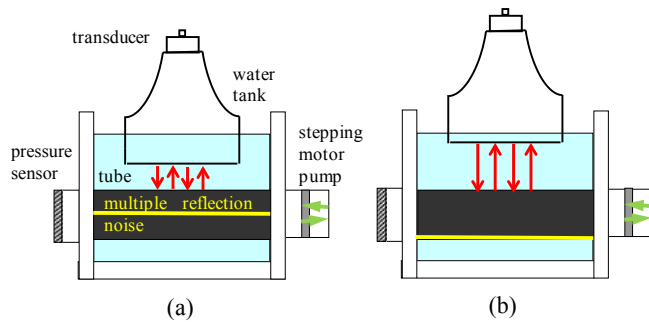


**Fig. 8.** (Color online) Arterial-wall-mimicking phantom made of silicone rubber tube pulsated by stepping motor pump. (a) Multiple-reflection noise inside the lumen. (b) Multiple-reflection noise on the posterior wall.

where  $W$  is an empirical constant, which is sufficiently smaller than  $\pi/2$ . Secondly, in the case that  $n = 0$  or  $1$ , the aliasing number  $n$  is determined so that the following  $e(n)$  was minimized:

$$e(n) = |\theta_{\text{harm}} + 2\pi n - 2\theta_{\text{fund}}|. \quad (6)$$

The corrected  $\theta_{\text{harm}}$  is expressed by  $\theta_{\text{harm}} + 2\pi n$ . The phase shift values of the harmonic, the fundamental, and the corrected harmonic are shown in Figs. 7(a)–7(c), respectively. In Fig. 7(c), aliasing in Fig. 7(a) was corrected. The corrected phase shift  $\theta_{\text{harm}} + 2\pi n$  was applied to the phased-tracking method.<sup>15,16)</sup>

### 3. Results

To evaluate the accuracy of the proposed method, we prepared a phantom mimicking the arterial wall made of a silicone rubber tube, which was pulsated by a stepping motor pump. The internal pressure was measured using a pressure sensor (Keyence GP-M001). The wall thickness of the silicone rubber tube was 1.1 mm and the inner diameter was 8 mm, which were similar to those of the common carotid artery. The material of the silicone rubber tube included graphite powder (weight ratio, 5%) to scatter ultrasound.

To evaluate the influence of the multiple-reflection noise generated between the anterior wall and the transducer on the posterior wall, the distance from the transducer to the tube was controlled, as shown in Fig. 8. Figure 8(a) shows the position where the multiple-reflection noise generated between the transducer and the anterior wall appeared inside the lumen, and Fig. 8(b) shows the position where the multiple-reflection noise appeared only on the posterior wall.

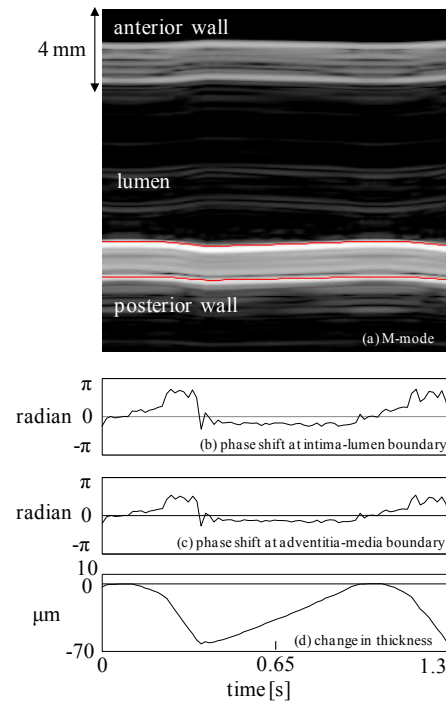


**Fig. 9.** (Color online) Arterial-wall-mimicking phantom results of the fundamental method with the multiple-reflection noise inside lumen. (a) Magnified M-mode image with the posterior wall boundary tracking results overlaid. (b) Phase shift at the intima–lumen boundary. (c) Phase shift at the adventitia–media boundary. (d) Change in thickness of the posterior wall.

In Fig. 8(b), the distance between the transducer and the posterior wall was controlled to be twice that between the transducer and the anterior wall.

The change in thickness and elasticity were compared between the fundamental and PI methods. The transmitting center frequency of the PI method is chosen to be about half of that of the fundamental method. The transmitting and detection center frequencies for the fundamental method were 11.5 and 11 MHz, respectively. Those for the PI method were 5.7 and 11 MHz for harmonic components and 5.5 MHz for fundamental components, respectively. Since the motion of the wall of the phantom was slower than that of the human carotid artery, to validate how the proposed method prevents aliasing noise, the frame rates in this experiment were set to 66.7 Hz for the fundamental method and 33.4 Hz for the PI method.

Figure 9 shows the results obtained by the fundamental method, in which the multiple-reflection noise was inside the lumen. Figure 9(a) shows a magnified M-mode image overlaid with the tracking results at the posterior wall boundary. We can see that the multiple-reflection noise appeared inside the lumen clearly. Figures 9(b)–9(d) show the phase shift at the intima–lumen boundary, the phase shift at the adventitia–media boundary, and the change in thickness of the posterior wall, respectively. In Fig. 9(d), when the posterior wall was closest to the transducer, the change in thickness was set to zero. The maximum change in thickness was 62.0  $\mu\text{m}$  and  $E_\theta$  was estimated as 298 kPa by Eq. (4).

Figure 10 shows the results of the fundamental method, in which the multiple-reflection noise was only on the posterior wall. Figure 10(a) shows a magnified M-mode image over-

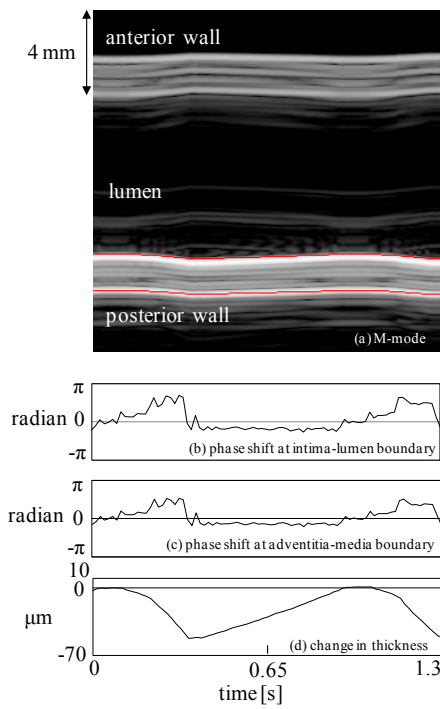


**Fig. 10.** (Color online) Arterial-wall-mimicking phantom results of the fundamental method with the multiple-reflection noise on the posterior wall. (a) Magnified M-mode image with the posterior wall boundary tracking results overlaid. (b) Phase shift at the intima–lumen boundary. (c) Phase shift at the adventitia–media boundary. (d) Change in thickness of the posterior wall.

laid with the tracking results of the posterior wall boundary. We can see the multiple-reflection noise appeared only on the posterior wall clearly. Figures 10(b)–10(d) show the phase shift at the intima–lumen boundary, the phase shift at the adventitia–media boundary, and the change in thickness of the posterior wall, respectively. The maximum change in thickness was  $52.3\ \mu\text{m}$  and  $E_\theta$  was estimated as 353 kPa using Eq. (4).

Figure 11 shows the results obtained by the proposed method, in which the multiple-reflection noise was inside the lumen, which corresponds to Fig. 9. Figure 11(a) shows a magnified M-mode image overlaid with the tracking results of the posterior wall boundary. The multiple-reflection noise was much more suppressed than that generated in the fundamental method. Figures 11(b)–11(d) show the corrected phase shift at the intima–lumen boundary, the corrected phase shift at the adventitia–media boundary and the resultant change in thickness of the posterior wall, respectively. In Figs. 11(b) and 11(c), the scale of the phase was expanded to  $3\pi/2$  since the phase of the harmonic component was corrected in the range from  $-2\pi$  to  $2\pi$  using the proposed method. The maximum change in thickness was  $61.1\ \mu\text{m}$  and  $E_\theta$  was estimated as 302 kPa using Eq. (4).

Figure 12 show the results obtained by the phase shift correction method used in Figs. 11(b) and 11(c). The harmonic component results are shown in Figs. 12(a), 12(b), and 12(c); the fundamental component results are shown in Figs. 12(d), 12(e), and 12(f); and the corrected harmonic results are shown in Figs. 12(g), 12(h), and 12(i). Figures 12(a), 12(d), and 12(g) show magnified M-mode images overlaid with the tracking results of the posterior wall

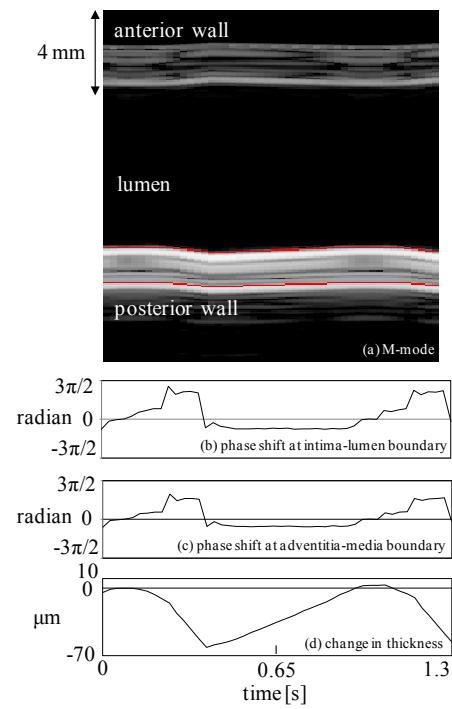
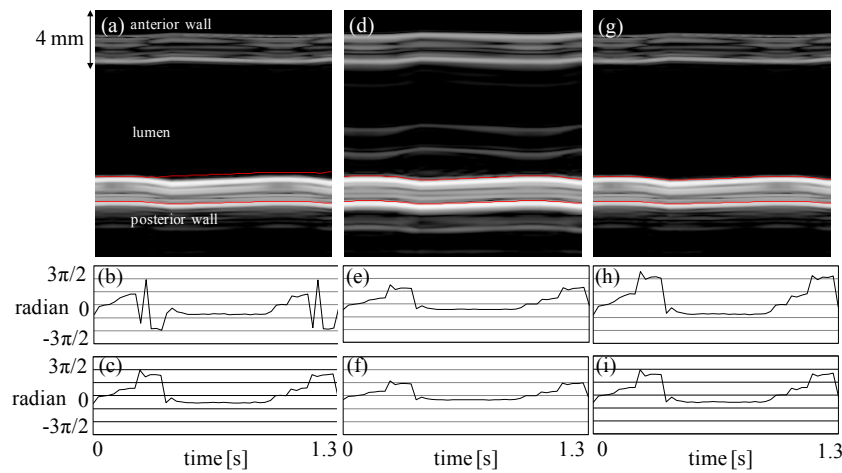


**Fig. 11.** (Color online) Arterial-wall-mimicking phantom results of the PI method with the multiple-reflection noise inside lumen. (a) Magnified M-mode image with the posterior wall boundary tracking results overlaid. (b) Corrected phase shift at the intima–lumen boundary. (c) Corrected phase shift at the adventitia–media boundary. (d) Change in thickness of the posterior wall.

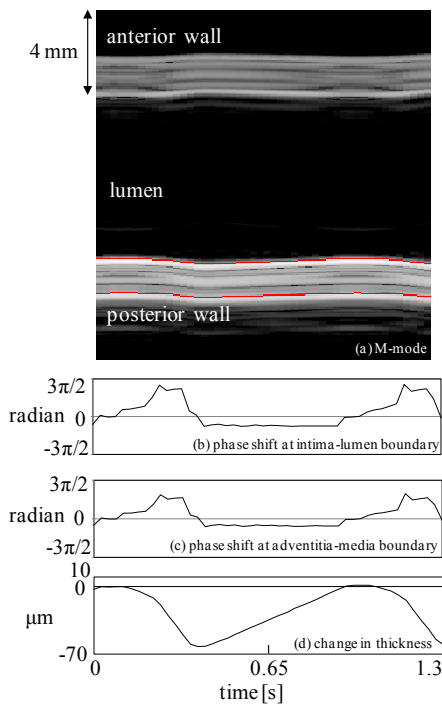
boundary. Figures 12(b), 12(e), and 12(h) show the phase shift at the intima–lumen boundary. Figures 12(c), 12(f), and 12(i) show the phase shift at the adventitia–media boundary. Aliasing noise is shown in Fig. 12(b) and apparent tracking error of the intima–lumen boundary is shown in Fig. 12(a). It is shown that aliasing noise was corrected in Fig. 12(h) and the intima–lumen boundary was successfully traced in Fig. 12(g).

Figure 13 shows the results of the proposed method, in which the multiple-reflection noise was only on the posterior wall, which corresponds to Fig. 10. Figure 13(a) shows a magnified M-mode image overlaid with the tracking results at the posterior wall boundary. The multiple-reflection noise is much more suppressed than that generated in the fundamental method. Figures 13(b), 13(c), and 13(d) show the corrected phase shift at the intima–lumen boundary, the corrected phase shift at the adventitia–media boundary, and the change in thickness of the posterior wall, respectively. In Figs. 13(b) and 13(c), the scale of the phase was expanded to  $3\pi/2$ . The maximum change in thickness was  $62.2\ \mu\text{m}$  and  $E_\theta$  was estimated as 297 kPa using Eq. (4).

Figure 14 shows the phase shift correction method used in Figs. 13(b) and 13(c). The harmonic component results are shown in Figs. 14(a), 14(b), and 14(c), the fundamental component results are shown in Figs. 14(d), 14(e), and 14(f) and the corrected harmonic results are shown in Figs. 14(g), 14(h), and 14(i). Figures 14(a), 14(d), and 14(g) show magnified M-mode images overlaid with the tracking results at the posterior wall boundary. Figures 14(b), 14(e), and 14(h) show the phase shifts at the intima–lumen boundary. Figures 14(c), 14(f), and 14(i) show the phase shift at the



**Fig. 12.** (Color online) Phase shift of the correction method with the multiple-reflection noise inside lumen. (a) Magnified M-mode image of harmonic component with the posterior wall boundary tracking results overlaid. (b) Phase shift of harmonic component at the intima–lumen boundary. (c) Phase shift of harmonic component at the adventitia–media boundary. (d) Magnified M-mode image of fundamental component with the posterior wall boundary tracking results overlaid. (e) Phase shift of fundamental component at the intima–lumen boundary. (f) Phase shift of fundamental component at the adventitia–media boundary. (g) Magnified M-mode image of corrected harmonic component with the posterior wall boundary tracking results overlaid. (h) Phase shift of corrected harmonic component at the intima–lumen boundary. (i) Phase shift of corrected harmonic component at the adventitia–media boundary.



**Fig. 13.** (Color online) Arterial-wall-mimicking phantom results of the PI method with the multiple-reflection noise on the posterior wall. (a) Magnified M-mode image with the posterior wall boundary tracking results overlaid. (b) Corrected phase shift at the intima–lumen boundary. (c) Corrected phase shift at the adventitia–media boundary. (d) Change in thickness of the posterior wall.

adventitia–media boundary. Aliasing noise was shown in Fig. 14(b) and the apparent tracking error of the intima–lumen boundary was shown in Fig. 14(a). It is shown that aliasing noise was corrected in Fig. 14(h) and tracking of the intima–lumen boundary was obtained successfully in Fig. 14(g).

The change in the thickness and elasticity were almost the same in the case of the multiple-reflection noise inside the lumen shown in Fig. 11(d) and in the case of the multiple-

reflection noise on the posterior wall in the proposed method shown in Fig. 13(d). Furthermore, these results are almost the same as those of the fundamental method with the multiple-reflection noise inside the lumen as shown in Fig. 9(d). Only the results of the fundamental method with the multiple-reflection noise on the posterior wall show a smaller change in thickness and a larger elasticity, as shown in Fig. 10(d), which corresponds to a large error.

#### 4. Discussion

The conventional phased-tracking method utilizes the fundamental method. Although this method leads to precise elasticity measurement of the arterial wall if there is less noise on the posterior wall, it is not sufficient for elasticity measurements in a clinical setting since they contains various types of noises such as multiple-reflection noise. Only a few studies have been carried out on the influence of noise on the elasticity measurement. In the present study, we investigated the influence of the multiple-reflection noise on the accuracy of elasticity measurement.

To suppress multiple-reflection noise, the PI method was introduced. The suppression of multiple-reflection noise is discussed on the basis of the results of the experiment using the phantom mimicking the arterial wall, in which multiple-reflection noise in the lumen is as follows. Figures 15(a), 15(b), and 15(c) shows B-mode images obtained by the fundamental method (a) in which the transmitting center frequency was set at 11.4 MHz and the center detection frequency was set at 11 MHz, by the PI method (b) in which the transmitting center frequency was set at 5.7 MHz and the center detection frequency was set at 5 MHz, and by the PI method (c) in which the transmitting center frequency was set at 11 MHz, respectively. Figure 16 shows the received RF echoes and detected envelopes along the red vertical lines in Fig. 15. The power of the detected envelope under transmission and detection frequency conditions is shown in Fig. 17. The powers of the multiple-reflection noise at  $A_{22}$  in Fig. 17 of methods (a), (b), and (c) were  $-39.3$ ,  $-31.0$ , and

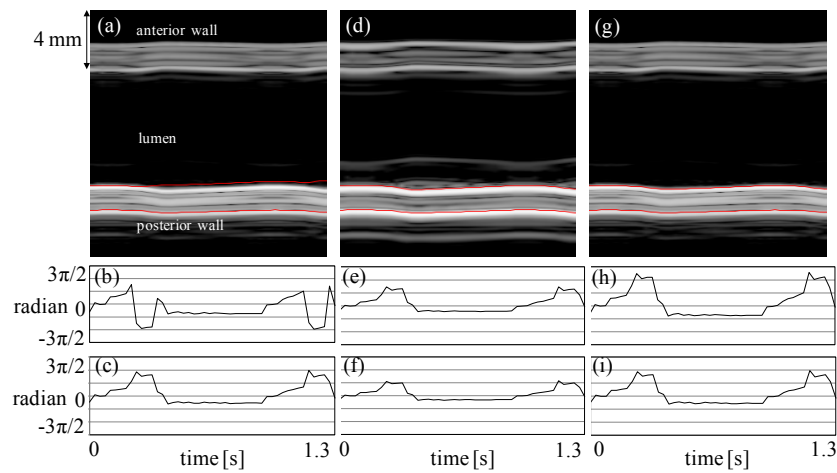


**Fig. 14.** (Color online) Phase shift correction method with the multiple-reflection noise on the posterior wall. (a) Magnified M-mode image of harmonic component with the posterior wall boundary tracking results overlaid. (b) Phase shift of harmonic component at the intima–lumen boundary. (c) Phase shift of harmonic component at the adventitia–media boundary. (d) Magnified M-mode image of fundamental component with the posterior wall boundary tracking results overlaid. (e) Phase shift of fundamental component at the intima–lumen boundary. (f) Phase shift of fundamental component at the adventitia–media boundary. (g) Magnified M-mode image of corrected harmonic component with the posterior wall boundary tracking results overlaid. (h) Phase shift of corrected harmonic component at the intima–lumen boundary. (i) Phase shift of corrected harmonic component at the adventitia–media boundary.

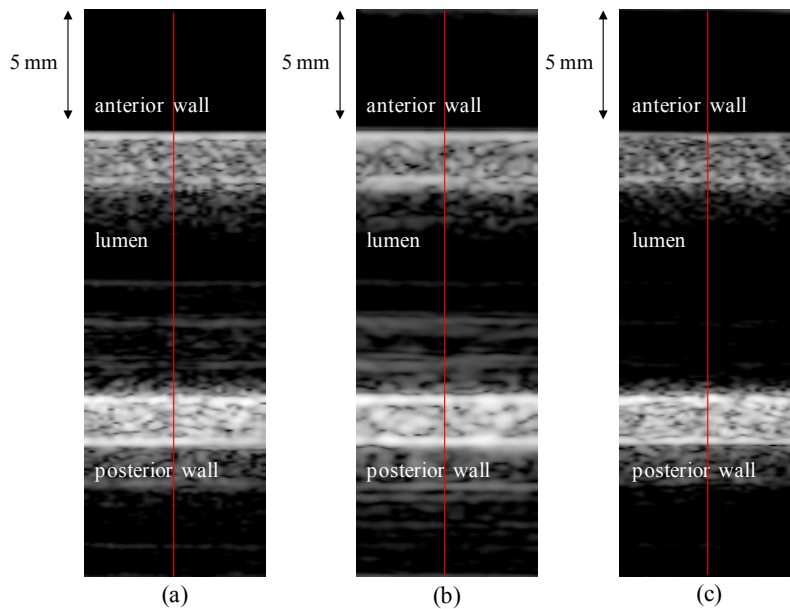


**Fig. 15.** (Color online) B-mode image of the arterial-wall-mimicking phantom in which multiple-reflection noise in the lumen. (a) Fundamental method. (b) PI method constructed from fundamental component. (c) PI method constructed from harmonic component.

−45.5 dB, respectively. It was shown that the multiple-reflection noise was highly suppressed in the PI method using a harmonic component. Possible reasons for the noise suppression mechanism are as follows. The generation of the harmonics component is in proportion to the square of the fundamental intensity based on nonlinear characteristics. The multiple-reflection noise arises from reflection from the anterior wall and reflection from the transducer surface. Since the depth of the anterior wall was small and defocused and the depth of the posterior wall was near a focused point of 1.5 cm, the generation of the harmonic component of the anterior wall was much less than that of the posterior wall. This mechanism could lead to the suppression of the multiple-reflection noise.

In the proposed method, the phase shift of harmonic quadrature demodulated signal  $\theta_{\text{harm}}$  is corrected on the

assumption that the phase shift of the harmonic quadrature demodulated signal  $\theta_{\text{harm}}$  is roughly equal to  $2\theta_{\text{fund}}$ . We investigated whether the assumption is valid even at a setting where the multiple-reflection noise is on the posterior wall. Figure 18 shows the experimental results when the harmonic component was not aliased. Figure 18(a) shows the phase shift of the harmonic component and that of the doubled fundamental component. The difference was small at each time and the maximum difference was 0.18 rad, which is much smaller than  $\pi/2$ , and the condition using Eq. (5) was satisfied. This may be a reason why the signal from the posterior wall is much stronger than that from the multiple-reflection noise. Although the phase differences were sufficiently small, the changes in position and thickness may be affected because they were obtained from the integral of the phase shift over one heartbeat. Figure 18(b) shows the

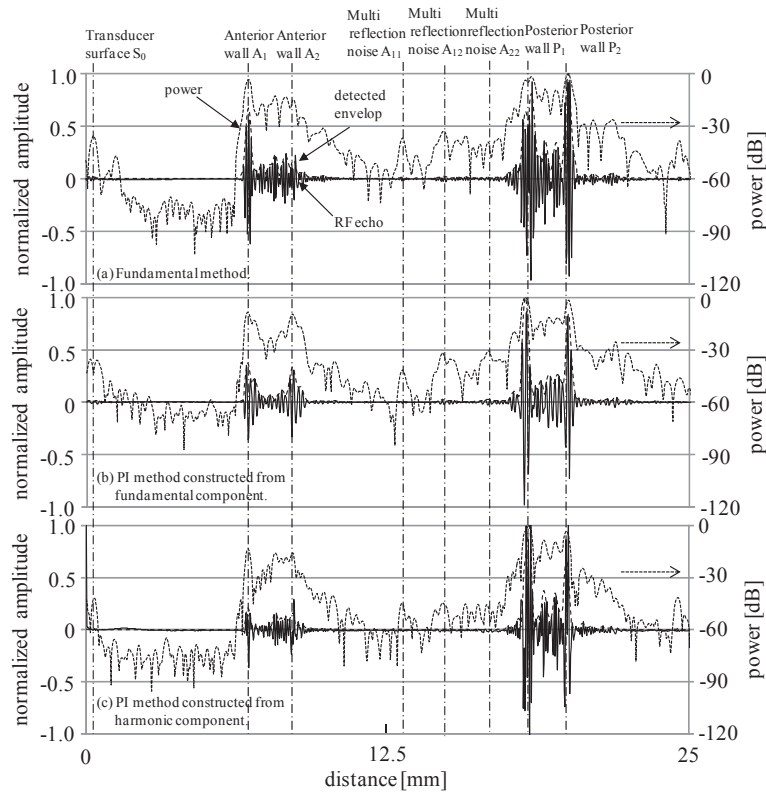


**Fig. 16.** RF echo and detected envelope. (a) Fundamental method. (b) PI method constructed from fundamental component. (c) PI method constructed from harmonic component.

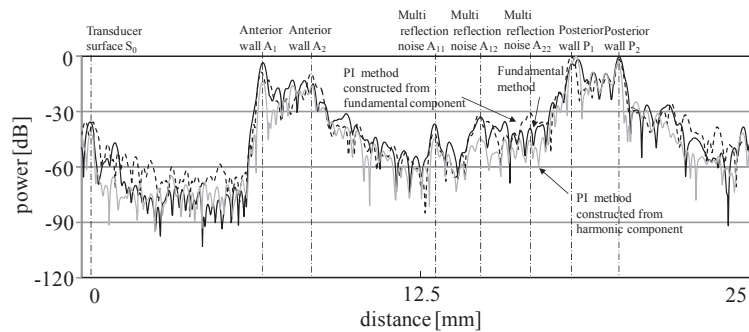


**Fig. 17.** Powers of the detected envelopes.

changes in position evaluated from the harmonic component and evaluated from the fundamental component. Figure 18(c) shows the difference between the changes in position and the maximum difference was 12.9  $\mu\text{m}$ . Although this 12.9  $\mu\text{m}$  difference was relatively smaller than the change in position, such as several hundred micrometers, it was not negligible in comparison with the change in thickness, such as several tens of micrometers. This reduction in the change in position could lead to the reduction in the change in thickness and increase in elasticity.

It was shown that the accuracy in the elasticity measurement was decreased in the fundamental method when the multiple-reflection noise was overlaid only on the posterior wall. By introducing the PI method, the correction of the phase shift of the harmonic component using the fundamental component prevented the tracking error of the arterial wall from aliasing owing to the reduced frame rate originating from the PI method. The accuracy in the elasticity measurement did not decrease for the PI method when the multiple-

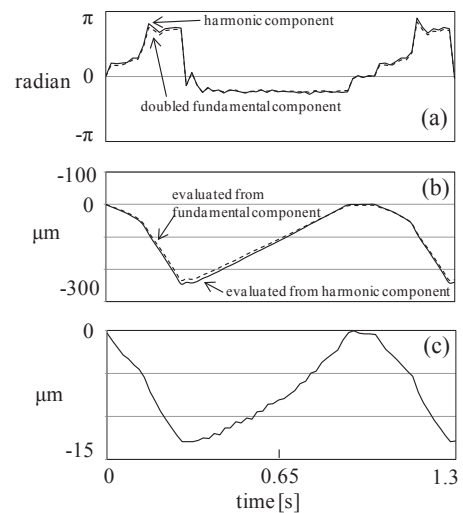


**Fig. 18.** (a) Phase shifts, (b) changes in position, and (c) difference between the changes in position at intima–lumen boundary with the multiple-reflection noise on the posterior wall.

reflection noise was only on the posterior wall. It is shown that it is important and effective to introduce a method to prevent the multiple-reflection noise on the posterior wall in the elasticity measurement of the arterial wall.

## 5. Conclusions

We have proposed a modified phased-tracking method using the PI method, in which aliasing of the phase shift of the harmonic component was corrected using that of the fundamental component. The PI method was applied to in vivo examination of carotid arteries and the detection frequencies were selected to increase the signal-to-noise ratios of the IMC of the posterior wall from the multiple-reflection noise inside the lumen. The improvement of the measurement of the arterial wall elasticity by the proposed method was validated using a phantom mimicking the arterial wall made of a silicone rubber tube pulsated by a stepping motor pump. The elasticity difference of the multiple-reflection noise on the posterior wall from that outside the posterior wall became much smaller when using the proposed method than when using the conventional method. It was shown that the proposed method is much more robust against multiple-reflection noise than the conventional method. The proposed method has potential use for measuring the elasticity of the arterial wall more accurately in the clinical setting than the conventional method.

- 1) H. Tanaka, M. Nishino, M. Ishida, R. Fukunaga, and K. J. Sueyoshi, *Stroke* **23**, 946 (1992).
- 2) R. T. Lee, A. J. Grodzinsky, E. H. Frank, R. D. Kamm, and F. J. Schoen, *Circulation* **83**, 1764 (1991).
- 3) H. M. Loree, A. J. Grodzinsky, S. Y. Park, L. J. Gibson, and R. T. Lee, *J. Biomech.* **27**, 195 (1994).
- 4) P. C. G. Simons, A. Algra, M. L. Bots, D. E. Grobbee, and Y. van der Graaf, *Circulation* **100**, 951 (1999).
- 5) S. Kageyama, H. Hasegawa, and H. Kanai, *Jpn. J. Appl. Phys.* **52**, 07HF04 (2013).
- 6) C. Arihara, H. Hasegawa, and H. Kanai, *Jpn. J. Appl. Phys.* **45**, 4727 (2006).
- 7) T. Kaneko, H. Hasegawa, and H. Kanai, *Jpn. J. Appl. Phys.* **46**, 4881 (2007).
- 8) K. Kitamura, H. Hasegawa, and H. Kanai, *Jpn. J. Appl. Phys.* **51**, 07GF08 (2012).
- 9) Y. Nagai, H. Hasegawa, and H. Kanai, *Jpn. J. Appl. Phys.* **53**, 07KF19 (2014).
- 10) J. Blacher, R. Asmar, S. Djane, G. M. London, and M. E. Safar, *Hypertension* **33**, 1111 (1999).
- 11) Y. Miyachi, H. Hasegawa, and H. Kanai, *Jpn. J. Appl. Phys.* **54**, 07HF18 (2015).
- 12) P. Hallock, *Arch. Int. Med.* **54**, 770 (1934).
- 13) M. Saito, Y. Yamamoto, Y. Shibayama, M. Matsukawa, Y. Watanabe, M. Furuya, and T. Asada, *Jpn. J. Appl. Phys.* **50**, 07HF10 (2011).
- 14) H. Hasegawa, M. Sato, and T. Irie, *Jpn. J. Appl. Phys.* **55**, 07KF01 (2016).
- 15) H. Kanai, M. Sato, Y. Koiwa, and N. Chubachi, *IEEE Trans. Ultrason. Ferroelectr. Freq. Control* **43**, 791 (1996).
- 16) H. Kanai, H. Hasegawa, N. Chubachi, Y. Koiwa, and M. Tanaka, *IEEE Trans. Ultrason. Ferroelectr. Freq. Control* **44**, 752 (1997).
- 17) H. Hasegawa, H. Kanai, N. Hoshimiya, N. Chubachi, and Y. Koiwa, *Jpn. J. Appl. Phys.* **37**, 3101 (1998).
- 18) H. Hasegawa, H. Kanai, N. Hoshimiya, and Y. Koiwa, *Jpn. J. Appl. Phys.* **39**, 3257 (2000).
- 19) H. Hasegawa, H. Kanai, and Y. Koiwa, *Jpn. J. Appl. Phys.* **41**, 3563 (2002).
- 20) H. Hasegawa, H. Kanai, N. Chubachi, and Y. Koiwa, *Electron. Lett.* **33**, 340 (1997).
- 21) M. Cinthio, H. Hasegawa, and H. Kanai, *IEEE Int. Ultrasonics Symp. Proc.*, 2007, p. 997.
- 22) H. Hasegawa and H. Kanai, *Jpn. J. Appl. Phys.* **43**, 3197 (2004).
- 23) J. Inagaki, H. Hasegawa, H. Kanai, M. Ichiki, and F. Tezuka, *Jpn. J. Appl. Phys.* **44**, 4593 (2005).
- 24) J. Tang, H. Hasegawa, and H. Kanai, *Jpn. J. Appl. Phys.* **44**, 4588 (2005).
- 25) K. Ikeshita, H. Hasegawa, and H. Kanai, *Jpn. J. Appl. Phys.* **47**, 4165 (2008).
- 26) K. Ikeshita, H. Hasegawa, and H. Kanai, *Jpn. J. Appl. Phys.* **48**, 07GJ10 (2009).
- 27) K. Ikeshita, H. Hasegawa, and H. Kanai, *Jpn. J. Appl. Phys.* **50**, 07HF08 (2011).
- 28) K. Ikeshita, H. Hasegawa, and H. Kanai, *Jpn. J. Appl. Phys.* **51**, 07GF14 (2012).
- 29) M. Sato, H. Hasegawa, and H. Kanai, *Jpn. J. Appl. Phys.* **53**, 07KF03 (2014).
- 30) S. Miyashita, J. Murotsuki, J. Muromoto, K. Ozawa, N. Yaegashi, H. Hasegawa, and H. Kanai, *Ultrasound Med. Biol.* **41**, 1311 (2015).
- 31) Y. Sakai, H. Taki, and H. Kanai, *Jpn. J. Appl. Phys.* **55**, 07KF11 (2016).
- 32) G. F. Pinton, G. E. Trahey, and J. J. Dahl, *IEEE Trans. Ultrason. Ferroelectr. Freq. Control* **58**, 1272 (2011).
- 33) T. Yamamura, M. Tanabe, K. Okubo, and N. Tagawa, *Jpn. J. Appl. Phys.* **51**, 07GF01 (2012).
- 34) F. Tranquart, N. Grenier, V. Eder, and L. Pourcelot, *Ultrasound Med. Biol.* **25**, 889 (1999).
- 35) Q. Ma, Y. Ma, X. Gong, and D. Zhang, *Ultrasound Med. Biol.* **31**, 889 (2005).
- 36) D. H. Simpson, C. T. Chin, and P. N. Burns, *IEEE Trans. Ultrason. Ferroelectr. Freq. Control* **46**, 372 (1999).
- 37) C. C. Shen, Y. H. Chou, and P. C. Li, *J. Med. Ultrasound* **13**, 3 (2005).
- 38) J. R. Doherty, J. J. Dahl, and G. E. Trahey, *IEEE Trans. Ultrason. Ferroelectr. Freq. Control* **60**, 2347 (2013).